Extending the physics basis of quiescent H-mode toward ITER relevant parameters

W.M. Solomon[1], K.H. Burrell[2], M.E. Fenstermacher[3], A.M. Garofalo[2], B.A. Grierson[1], A. Loarte[4], G.R. McKee[5], R. Nazikian[1], T.H. Osborne[2], and P.B. Snyder[2]

[1]Princeton Plasma Physics Laboratory, Princeton, New Jersey 08543-0451, USA
[2]General Atomics, San Diego, California 92186-5608, USA
[3]Lawrence Livermore National Laboratory, Livermore, California 94551, USA
[4]ITER Organization, Route de Vinon-sur-Verdon - CS 90 046, 13067 St Paul Lez Durance Cedex, France
[5]University of Wisconsin-Madison, Madison, Wisconsin 53706, USA

E-mail: wsolomon@pppl.gov

Abstract. Recent experiments on DIII-D have addressed several long-standing issues needed to establish quiescent H-mode (QH-mode) as a viable operating scenario for ITER. In the past, QH-mode was associated with low density operation, but has now been extended to high normalized densities compatible with operation envisioned for ITER. Through the use of strong shaping, QH-mode plasmas have been maintained at high densities, both absolute ($\bar{n}_e \approx 7 \times 10^{19}$ m^{-3}) and normalized Greenwald fraction ($\bar{n}_e/n_G > 0.7$). In these plasmas, the pedestal can evolve to very high pressure and edge current as the density is increased. High density QH-mode operation with strong shaping has allowed access to a previously predicted regime of very high pedestal dubbed "Super H-mode". Calculations of the pedestal height and width from the EPED model are quantitatively consistent with the experimentally observed density evolution. The confirmation of the shape dependence of the maximum density threshold for QH-mode helps validate the underlying theoretical model of peeling-ballooning modes for edge localized mode (ELM) stability. In general, QH-mode is found to achieve ELM-stable operation while maintaining adequate impurity exhaust, due to the enhanced impurity transport from an edge harmonic oscillation, thought to be a saturated kink-peeling mode driven by rotation shear. In addition, the impurity confinement time is not affected by rotation, even though the energy confinement time and measured $E \times B$ shear are observed to increase at low toroidal rotation. Together with demonstrations of high beta, high confinement and low q_{95} for many energy confinement times, these results suggest QH-mode as a potentially attractive operating scenario for the ITER Q=10 mission.

PACS numbers: 52.55.Fa, 52.25.Fi, 52.30.Cv, 52.55.Tn

1. Introduction

Future burning plasma devices such as ITER [1] are typically designed assuming H-mode confinement, but require a plasma edge regime that keeps divertor heat loads to an acceptable level. However, standard H-mode is associated with steep gradients in the plasma edge forming the so-called pedestal, and these strong gradients are observed to trigger edge localized modes (ELMs) [2], resulting from exceeding the peeling-ballooning stability limit. Although ELMs prevent impurity accumulation in the core, they may lead to unacceptable peak divertor heat loads in a device such as ITER [3]. Therefore, significant effort is being spent to investigate external actuators to either eliminate or at least reduce the heat fluxes from ELMs, while retaining the positive benefits of impurity flushing without compromising the pedestal height or global confinement.

An ideal solution to eliminating ELMs is to utilize scenarios that are peeling-ballooning stable, but which still possess good H-mode confinement, such as quiescent H-mode (QH-mode) [4] or I-mode [5]. In QH-mode, the transport associated with ELMs is replaced by a benign "edge harmonic oscillation" (EHO) [4], or in some cases a more broadband form of MHD [6], which limits the plasma to just below the peeling-ballooning stability limit. The following sections cover recent advances in qualifying QH-mode as a possible operating scenario to meet ITER's $Q = 10$ mission. Specifically, section 2 describes efforts to extend QH-mode to high normalized fusion performance, and section 3 gives a summary of impurity transport driven by the EHO. In section 4, the extension of QH-mode to high density operation is described, leading to the experimental discovery of a new high pedestal regime dubbed "Super H-mode", discussed in section 5.

2. High normalized fusion performance in QH-mode

Recent experiments have extended QH-mode to high normalized fusion performance, $G = \beta_N H_{89}/q_{95}^2 \approx 0.36$ approaching the level required for $Q = 10$ performance on ITER ($G \approx 0.42$), with values for the confinement factor H_{89}, β_N and q_{95} sustained at ITER relevant values for many energy confinement times in an ITER similar plasma shape, as shown in figure 1. Here, H_{89} is the normalized confinement time relative to L-mode, q_{95} is the safety factor at the magnetic surface that encloses 95% of the toroidal flux, $\beta_N = \beta/(I_p/aB)$ is the normalized β, where $\beta =< p > /(B^2/2\mu_0)$ is the dimensionless plasma pressure, I_p the plasma current, a the minor radius and B the magnetic field.

To date, these results have been achieved in plasmas with significant counter neutral beam injection (NBI) torque. While QH-mode is robustly maintained at $\beta_N \approx 2$ through zero torque at $q_{95} \gtrsim 4.5$, increasing levels of (counter) NBI torque have been required to avoid locked modes as q_{95} is reduced, and at $q_{95} \approx 3.3$ it has proven difficult to reduce

the torque below about 2 Nm, as can be seen in figure 2. In general, QH-mode operation is maintained at low neutral beam torque through the use of non-axisymmetric fields, which have been found to drive the plasma toward the neoclassical "offset" rotation in the counter-I_p direction [7]. This technique enables the edge rotation shear, believed important for QH-mode operation, to be maintained in the absence of neutral beam torque. It should be noted that lower torque operation, if made stable, should actually improve the achieved performance, since the confinement in QH-mode is actually found to increase as the torque and rotation are reduced toward balanced torque injection [8].

Separately, experiments have tried to investigate the viability of accessing QH-mode with low NBI torque, since an outstanding question is whether non-axisymmetric fields can initiate the conditions for QH-mode without first spinning the plasma with counter NBI torque. Figure 3 shows that access to QH-mode at very low NBI torque may be achievable. In this example with $q_{95} > 4.5$, the L-H transition occurs around 1670 ms, followed by standard ELM-free H-mode. Non-axisymmetric $n = 3$ fields are applied using the DIII-D internal (I-coils), a set of 12 picture-frame coils inside the vacuum vessel, which begin ramping up at 1780 ms, and the first ELM occurs before the coils reach their programmed maximum. Following this first ELM, the plasma begins to exhibit weak broadband MHD activity characteristic of some QH-modes, ELMs are absent and the density becomes better regulated. During this period of broadband MHD lasting approximately 200 ms, the plasma achieves $\beta_N \approx 1.6$ and confinement factor $H_{98(y,2)} \approx 1.1$ relative to the IPB98(y,2) H-mode scaling [9]. Although the broadband MHD persists longer, in this case it appears inadequate to provide sufficient particle transport; density continues to rise, and ELMs eventually return. Shortly thereafter, a locked mode is encountered, similar to the low torque high G plasmas. Clearly much more work is required to enable robust QH-mode access at low torque. Note that this example only used low levels of $n = 3$ fields; earlier attempts to try to maximize the $n = 3$ field had been less successful, typically triggering locked $n = 1$ modes even earlier in the discharge.

Recent analysis has indicated that the challenges to low torque operation may, in part, be the result of a large $n = 1$ error field that is introduced together with the desired $n = 3$ field from the coils [10]. While the vacuum $n = 1$ field is very small, there is significant amplification of this field in the plasma. Future experiments will investigate whether the limitation in low torque, low q_{95} QH-mode can be overcome with improved error field compensation and optimization of the safety factor profile.

3. Impurity transport driven by the EHO

Adequate transport of impurities is essential for maintaining a high fuel-ion ratio and high performance. In standard ELMing H-mode, impurity accumulation is avoided by the periodic particle expulsion with each ELM. However, since ELM mitigated or suppressed regimes are required for ITER to prevent excessive thermal damage to plasma facing components, it is critical that any solution for the large heat fluxes also be consistent with adequate impurity transport.

Measurement of particle transport is complicated due to uncertainties in the particle source terms, particularly due to recycling from the wall. Therefore, impurity transport measurements are best made using a species that is not typical in the tokamak and does not recycle. For these studies, carbon tetrafluoride (CF_4) was injected into the plasma, with charge exchange recombination (CER) spectroscopy measuring the F-IX (10-9) transition at 4796 Å. The impurity confinement time τ_P is readily determined from the exponential decay of the signal [11].

Figure 4 shows an example of the uptake and exhaust of F impurity following a 5 ms gas puff of CF_4. A database of discharges shows a dependence of the F impurity confinement time on the density for both QH-mode and ELMing discharges. One finds that at comparable densities, the QH-mode plasmas have impurity confinement times at least as short as regular ELMing plasmas with ELM frequency about 40 Hz.

As previously noted, QH-mode plasmas exhibit increased energy confinement as the torque and rotation are reduced. Importantly, τ_P is found to be insensitive to the rotation, such that τ_P/τ_E actually decreases in the more reactor relevant range of low rotation (figure 4). Similar studies have also shown that τ_P is insensitive to the level of applied non-axisymmetric field [11]. Future experiments will attempt to look at higher Z transport, perhaps using either an insertable sample or through injection of higher Z pellets by utilizing a modification to the Lithium Granule Injector on DIII-D.

4. Extension of QH-mode to ITER relevant densities

QH-mode has historically been associated with low density operation (typically $\bar{n}_e/n_G < 0.4$, where $n_G = I_p/\pi a^2$ is the Greenwald density limit for tokamaks [12]), and indeed, the general recipe for achieving robust QH-mode has been to work on limiting the fueling and reducing the density. While QH-mode operation is therefore associated with low collisionality as envisioned in a future reactor, the low normalized density associated with QH-mode has been an outstanding criticism about the applicability of the scenario to a device like ITER.

Peeling-ballooning theory predicts that shaping should provide one of the strongest

control parameters for affecting the maximum tolerable density in QH-mode [13]. The EHO is believed to be the saturated state of a current-driven mode encountered near the kink-peeling stability boundary, for which rotation shear is destabilizing [13]. Therefore, operation along the low-n kink-peeling boundary is thought to be an essential requirement for access to QH-mode. Experimentally, plasmas with an EHO are always found to exist along this boundary. At low triangularity, operation along the kink-peeling boundary is only possible at very low pedestal densities, with higher density and collisionality driving the plasma toward the high-n ballooning boundary. With stronger shaping, the stability boundary is calculated to widen, allowing QH-mode operation at higher densities [13].

Experiments were conducted to investigate the upper limits in density for QH-mode operation [14]. In particular, gas puffing was added during the QH-mode phase, controlled via density feedback to follow a pre-programmed target with a density ramp. In this way, the maximum tolerable density compatible with QH-mode was determined as indicated by the return of ELMs at high density. An example of this is shown in figure 5, where a high density QH-mode is contrasted with typical QH-mode plasma where little if any D_2 gas is injected. This prescription produces a strong EHO and the cleanest QH-mode operation.

The data confirms that stronger shaping allows higher density QH-mode in a scan of the minimum in the upper and lower triangularity of the plasma shape, $\delta \equiv \min(\delta_{\text{upper}}, \delta_{\text{lower}})$, with other key parameters such as toroidal field, plasma current and heating power held constant (figure 6). This data shows that plasmas with high triangularity can sustain QH-mode at double the Greenwald fraction compared to plasmas with reduced triangularity (in the high triangularity case, the Greenwald fraction is $\bar{n}_e/n_G > 0.7$). This demonstrates that QH-mode can be obtained over a wide range of plasma density. Note that in almost all cases, core MHD was triggered before the first ELM at high density and high triangularity. Therefore, while the data in figure 6 is the maximum QH-mode density experimentally achieved, it need not represent an absolute limit to QH-mode operation, at least as far as peeling-ballooning theory is concerned. Further work is needed to understand how core instabilities might couple to the pedestal and influence QH-mode performance.

With strong shaping, the QH-mode pedestal pressure is found to evolve to levels comparable with some of the highest performance transient pedestals seen on DIII-D. At fixed β_N, maintained with feedback control of the neutral beam power, the height, width and gradient of the pedestal pressure all increase as the density increases, as shown in figure 7, and the increase in the density originates from the pedestal rather than via a central peaking of the density profile.

Examples of the measured profiles and their fits are shown in figure 8. Here, the total pressure is estimated as the contribution from the sum of the electron and ion pressures, together with a contribution from the beam ions (calculated using the Monte Carlo code NUBEAM [15] within the ONETWO [16] transport code). One sees a significant range in pedestal density over which QH-mode conditions are maintained. Note that the pedestal temperature decreases, although by a lesser extent than the rise in density, such that the overall pedestal pressure increases with density.

Calculations of the expected pedestal evolution from EPED [17] are quantitatively consistent with the experimental measurements [14]. Similar EPED calculations using the ITER shape and other expected parameters find that the ITER pedestal will operate on the kink-peeling boundary where QH-mode can exist for all pedestal densities up to values exceeding 10^{20} m^{-3}, which is significantly higher than the baseline ITER $Q = 10$ scenario requirement [18].

Previous studies have indicated that the fusion power increases roughly as the square of the pedestal pressure [19]. However, these studies have been performed at fixed pedestal density, such that the rising pedestal pressure was due to an increase in temperature. Contrast that to the present work, where the pedestal height increase comes from the density, even as the temperature is in fact reduced. Preliminary simulations of the impact of increasing the pedestal density subject to the EPED constraint on the pressure have been performed for ITER plasmas. Using the GLF23 model [20] within TRANSP, it is found that the D-T reaction rate and the overall fusion power still increase with pedestal density, but the improvement in fusion power is closer to linear, with the reduced ion temperature lowering the fusion reactivity and offsetting some of the potential gain seen in earlier studies.

5. Access to Super H-mode

Application of the EPED model has revealed that a second region of ELM-stable operation is possible in strongly shaped plasmas at high density, characterized by very high pedestal pressure. In general, the pedestal height is limited due to coupled current-driven peeling modes and pressure-driven ballooning modes. However, improved stability is possible due to a decoupling of these modes that occurs with strong plasma shaping. At high triangularity, a valley of improved pedestal stability is theoretically predicted to open at high density, giving rise to a new regime dubbed "Super H-mode" [21]. Obtaining this high pedestal state is a challenge because at fixed density, the plasma will encounter the lower pedestal solution first, preventing access to the high pedestal pressures predicted by EPED.

A time-evolving density trajectory in QH-mode, shown in figure 9, appears to

have overcome this problem and accessed the Super H-mode regime [14]. For pedestal densities above approximately 6×10^{19} m^{-3}, EPED finds two separate regions for ELM stable operation, as evident in the plot of total pedestal pressure (including thermal and fast ion contributions) versus the electron pedestal density in figure 10. By first establishing QH-mode at low collisionality, it has been possible to traverse along the kink-peeling boundary and enter a channel of high pedestal pressure, avoiding the lower pedestal pressure solution. Eventually, the plasma begins ELMing regularly, the plasma exits the Super H-mode channel and the pedestal drops down to the lower pressure solution, resulting in nearly a factor of two reduction in the pedestal pressure with only a modest change in density. Therefore, the experimental trajectory in figure 9 demonstrates a bifurcation in the pedestal height at high density, as predicted by EPED.

The thermal energy confinement time is found to increase as the density and pedestal pressure evolve to higher values, as seen in figure 11(a). Here, the thermal energy confinement time is computed from the measured density and temperature profiles and the neutral beam power and fast ion energy content calculated with TRANSP [22]. The confinement time rises more than 50% before a $m/n = 3/2$ tearing mode is destabilized, reducing the core confinement. In general, increasing thermal energy confinement would be expected in a plasma with increasing pedestal pressure and stiff core transport. Indeed, the total thermal stored energy increases primarily due to the contribution from the pedestal, although the core also increases somewhat [figure 11(b)]. Therefore, the strong gas puffing used to fuel the plasma and raise the pedestal pressure does not necessarily lead to a degradation of core confinement. More detailed transport analysis confirms that the core thermal transport is actually slightly reduced. Calculations with the transport model TGLF at various times during the density ramp also show that the core transport is relatively stiff, with thermal diffusivities remaining essentially constant independent of the pedestal pressure (figure 12).

Although the possible advantage in exploiting the Super H-mode regime is apparent, it should be clearly noted that the core mode shown in figure 11 is triggered before the plasma enters the Super H-mode channel. Therefore, even though the stored energy associated with the pedestal continues to improve, the full potential of the Super H-mode regime is not realized in this case, and addressing core instabilities remains a challenge to be overcome.

The confinement factor $H_{98(y,2)}$ remains constant as the pedestal rises, even with a significant improvement in the thermal energy confinement. At first, this seems counterintuitive; one might expect the H-factor to increase if the thermal stored energy increases without the need of additional heating power. However, the IPB98(y,2)

scaling contains a strong density dependence ($n_e^{0.41}$) as determined from a multi-machine database, which appears to capture the increase in thermal energy confinement. To verify this, TRANSP simulations were performed using profiles from the early QH-mode phase (figure 10) as the starting point, from which the pedestal density was increased monotonically to very high values (well beyond that achieved in the experiment), while constraining the pedestal pressure according to the EPED solution as the boundary condition. Core profiles were then predicted with fixed input power and thermal diffusivity profiles . The results are shown in figure 13. Note that the plasma pressure profile becomes considerably broader at higher density and higher pedestal. The resultant computed $H_{98(y,2)}$ remains essentially constant over the entire density variation, despite the thermal energy and confinement increasing. Thus Super H-mode is not inherently a path to higher H-factors than typical H-mode. However, it does provide a path for maintaining H-mode levels of confinement at very high density (a favorable operating point for fusion) where standard H-mode typically deviates significantly from the IPB(98,y2) scaling.

The return of ELMs may be related to the loss of rotation shear [23], rather than an inherent transition from the current-driven kink-boundary to the pressure-driven ballooning-boundary. Reduced rotation and rotation shear arises due to two separate effects. Firstly, as a result of a reduction in the injected torque per particle as the density increases, with the moment of inertia of the plasma more than doubling from ≈ 5 Nms^2 to ≈ 11 Nms^2 over the range in pedestal covered in the discharge described by Fig. 9.Secondly, as a consequence of the increase in the co-current directed intrinsic torque [24, 25] as the pedestal gradients increase, which opposes the counter rotation driven by the counter-current beams used in these experiments. In this case, the intrinsic torque is calculated to more than double from 0.6 Nm to 1.3 Nm (making it a modest fraction of the angular momentum balance compared with counter-NBI torque > 4 Nm).More detailed analysis has found that the shear in $\omega_E = E_r/RB_\theta$, the rotation driven by the radial electric field E_r, may be the relevant quantity for QH-mode, and it appears that the plasma needs to be above an empirical threshold in order to maintain QH-mode conditions [8]. As shown in figure 14, the shear in ω_E is found to be already below the empirical boundary for QH-mode when the ELMs return.

Experiments have begun to exploit the enhanced Super H-mode pedestal by coupling it with a high performance core. In these plasmas, the global β_N was programmed to rise with the pedestal, as shown in Fig. 15. Plasmas with $H_{98(y,2)} > 1.2$, $\beta_{N,ped} \approx 1.2$, and $\beta_N > 3$ have been obtained, which represent the highest β_N achieved with a quiescent edge to date. For comparison, $\beta_{N,ped}$ anticipated for ITER is typically around 0.7. Typical of all higher β Super H-mode attempts, there is a competition

between the transport from the EHO and the need to go to higher pedestal density. One sees dramatic changes in the pedestal density evolution as the EHO mode number and intensity change, and in fact the Super H-mode regime is reached when the coherent EHO abruptly ends and is replaced with broadband MHD that exhibits less efficient particle transport [26]. Therefore, fully exploiting this regime requires the careful balancing of the fueling and the EHO driven transport: too strong an EHO keeps the pedestal density down, while too weak an EHO is insufficient to prevent an ELM, leading to the exit from the Super H-mode channel.

Figure 16 shows a comparison between the experimental pedestal parameters with the EPED model predictions for a similar high β_N Super H-mode discharge. These higher β variants of Super H-mode do not move further into Super H-mode than the earlier modest β ones, and the challenge remains how to move deep into the Super H regime and stay there, since unlike an L-H transition, the real advantage realized in Super H-mode is a function of how far up the improved stability channel we can successfully navigate.

6. Conclusions

Recent experimental work in QH-mode plasmas on DIII-D suggests that it may be the most attractive operating scenario for achieving ITER's Q=10 mission. It exhibits inherently ELM-stable operation at ITER relevant values of β_N, H_{89}, q_{95}, torque and density (although not yet all simultaneously). Low q_{95} operation at high normalized fusion performance remains hampered by locked modes, and future efforts will investigate improved error field correction and modifications to the q-profile to try to overcome this limitation. Experiments have demonstrated that QH-mode can maintain adequate impurity transport to prevent low-Z impurity accumulation, exhibiting transport levels comparable to plasmas with 40 Hz ELMs, a frequency considerably higher than seen in DIII-D ITER baseline discharges. In the future, these impurity studies will be extended to higher-Z impurities, of particular concern for metal-wall machines. Guided by theory, QH-mode has been extended to high normalized densities comparable to that required for ITER. This helps validate the model for the EHO, although work remains to establish the scaling of the EHO to ITER; both for destabilizing the EHO as well as characterizing whether the transport is sufficient to prevent ELMs. Finally, QH-mode has provided a path to the Super H-mode regime with very high pedestals, and has permitted QH-mode operation at high β_N and $\beta_{N,ped}$. If successfully exploited, Super H-mode may open the path to much higher performance in a fusion reactor than currently achievable in standard H-mode, but considerably more effort is required to determine exactly how far up the predicted channel it is possible to

navigate while avoiding both core and pedestal instabilities.

This material is based upon work supported by the U.S. Department of Energy, Office of Science, Office of Fusion Energy Sciences, using the DIII-D National Fusion Facility, a DOE Office of Science user facility, under Awards DE-AC02-09CH11466, DE-FC02-04ER54698, DE-FG02-95ER54309, DE-AC52-07NA27344, DE-FG02-89ER53296, and DE-FG02-08ER54999. DIII-D data shown in this paper can be obtained in digital format by following the links at https://fusion.gat.com/global/D3D_DMP. The views and opinions expressed herein do not necessarily reflect those of the ITER Organization.

[1] Shimada M *et al* Progress in the ITER Physics Basis Chapter 1: Overview and summary 2007 Nucl. Fusion **47** S1

[2] Zohm H. 1996 Plasma Phys. Control. Fusion **38** 105

[3] Loarte A. *et al* 2003 Plasma Phys. Control. Fusion **45** 1549

[4] Burrell K.H. *et al* 2001 Phys. Plasmas **8** 2153

[5] Whyte D.G. *et al* 2010 Nucl. Fusion **50** 105005

[6] Burrell K.H. *et al* 2005 Phys. Plasmas **12** 056121

[7] Garofalo A.M. *et al* 2008 Phys. Rev. Lett. **101** 195005

[8] Garofalo A.M. *et al* 2011 Nucl. Fusion **51** 083018

[9] ITER Physics Expert Groups on Confinement and Transport and Confinement Modelling and Database, ITER Physics Basis Editors 1999 Nucl. Fusion **39** 2175

[10] Garofalo A.M. *et al* 2015 "The Quiescent H-mode regime for high performance ELM-stable operation in future burning plasmas," to be submitted to Phys. Plasmas

[11] Grierson B.A. *et al* 2014 Nucl. Fusion **54** 114011

[12] Greenwald M. 2002 Plasma Phys. Control. Fusion **44** R27

[13] Snyder P.B. *et al* 2007 Nucl. Fusion **47** 961

[14] Solomon W.M. *et al* 2014 Phys. Rev. Lett. **113** 135001

[15] Pankin A. *et al* 2004 Phys. Commun. **159** 157

[16] St John H.E. *et al* 1994 in *Proc.15th International Conf. on Plasma Physics and Controlled Nuclear Research* (Seville, Spain) (IAEA, Vienna, 1995) Vol 3, p603

[17] Snyder P.B. *et al* 2009 Phys. Plasmas **16** 056118

[18] Burrell K.H. *et al* 2012 Phys. Plasmas **19** 056117

[19] Kinsey J.E. *et al*, 2011 Nucl. Fusion **51**, 083001

[20] Kinsey J.E. *et al.* 2003 Fusion Sci. Technol. **44** 763

[21] Snyder P.B. *et al* 2012 Proc. 24th Int. Conf. (San Diego, CA) (Vienna: IAEA) CD-ROM file th_p3-17.pdf and http://www-naweb.iaea.org/napc/physics/FEC/FEC2012/html/fec12.htm

[22] Hawryluk R.J. 1980 in *Phys. Plasmas Close to Thermonuclear Conditions*, edited by B. Coppi *et al* (CEC, Brussels, 1980), Vol 1, p 19.

[23] Burrell K.H. *et al* 2009 Phys. Rev. Lett. **102** 155003

[24] Solomon W.M. *et al* 2010 Phys. Plasmas **17** 056108

[25] Solomon W.M. *et al* 2011 Nucl. Fusion **51** 073010

[26] Grierson B.A. *et al* 2014 "Impurity confinement and transport in high confinement regimes without ELMs on DIII-D," submitted to Phys. Plasmas

Figure 1. (Color online) High performance QH-mode: (a) β_N; (b) H_{89} factor; (c) D_α brightness and; (d) normalized fusion performance $G = \beta_N H_{89}/q_{95}^2$. ITER target values for $Q = 10$ operation is shown by the dotted lines.

Figure 2. (Color online) The torque required for stable operation is seen to increase as q_{95} decreases. (a) β_N, and (b) neutral beam torque. The approximate time of locking is indicated by the dashed vertical line for the lower q_{95} values and the corresponding torque at those times is also shown by the solid circles.

Figure 3. (Color online) QH-mode with low torque startup. (a) β_N, H_{98} and torque $T_{\rm inj}$; (b) Pedestal density and D_α light; (c) I-coil current; (d) Spectrogram with toroidal modal number identification from magnetics measurements.

Figure 4. (Color online) (a) F emission measured by CER following injection of CF_4. (b) Ratio of τ_P/τ_E as a function of the angular momentum in QH-mode plasmas, scanned here through controlled variation of the neutral beam torque.

Figure 5. (Color online) Density, gas, D_α light and magnetic spectrogram for typical QH-mode (left), and QH-mode with a density ramp achieved with gas puffing (right).

Figure 6. (Color online) Maximum attainable QH-mode Greenwald fraction as a function of triangularity at fixed plasma current and toroidal field.

Figure 7. (Color online) Evolution of QH-mode during density ramp by gas puffing. (a) Pedestal height; (b) pedestal width $\Delta\rho$, where ρ is the normalized minor radius; (c) Pedestal gradient; and (d) line average and pedestal density.

Figure 8. (Color online) QH-mode pedestal profiles at low (red) and high (green) density: (a) electron density; (b) carbon concentration; (c) electron temperature; (d) ion temperature; (e) electron pressure; (f) total pressure. The full radial profiles are shown as an inset in the upper right of each panel.

Figure 9. (Color online) Time evolution of QH-mode plasma as density is raised with gas puffing: (a) Pedestal density; (b) Pedestal electron pressure; and (c) D_α brightness.

Figure 10. (Color online) Plot of total pedestal pressure as a function of pedestal electron density, overlain onto EPED prediction, showing evolution of QH-mode pedestal from figure 9 into Super H-mode regime of high pedestal and bifurcation to lower pedestal ELMing state.

Figure 11. (Color online) (a) Thermal energy confinement time and $n = 2$ amplitude; (b) thermal energy content; and (c) D_α light.

Figure 12. (Color online) Time histories (corresponding to increasing density) of the ion and electron thermal diffusivities at different radii.

Figure 13. (Color online) TRANSP prediction of a simulated, prescribed increase in pedestal density following the EPED solution, using fixed thermal diffusivity . Time histories for: (a) pedestal pressure (kPa) and pedestal density ($\times 10^{19}$ m^{-3}); (b) Total and thermal stored energy (MJ); (c) Ion and electron temperature (keV); (d) H_{98} and thermal energy confinement time (s). Profiles at low and high pedestal density, corresponding to 2.1 and 2.9 s in the simulation: (e) Plasma pressure (kPa); (f) electron density ($\times 10^{19}$ m^{-3}); (g) electron temperature (keV); and (h) ion temperature (keV).

Figure 14. (Color online) Edge shear of impurity rotation Ω versus edge shear in $\omega_E = E_r/RB_\theta$ (both normalized to the Alfvén rotation speed ω_A), evaluated at the outer half of the pedestal, at different times in the QH-mode to Super H-mode evolution. The empirical boundary established in reference [8] is indicated by the dashed line. Standard QH-mode is shown with blue circles, while the Super H periods are indicated by green triangles

Figure 15. (Color online) Super H-mode at higher β_N. (a) Global and pedestal β_N; (b) pedestal density; (c) D_α light; and (d) magnetic spectrogram. The period when the plasma is in the Super H channel is indicated with the shading.

Figure 16. (Color online) Comparison of EPED model predictions for the pedestal height versus pedestal density, compared with experimental measurements at two times, early in standard QH-mode and later in the Super H-mode channel.

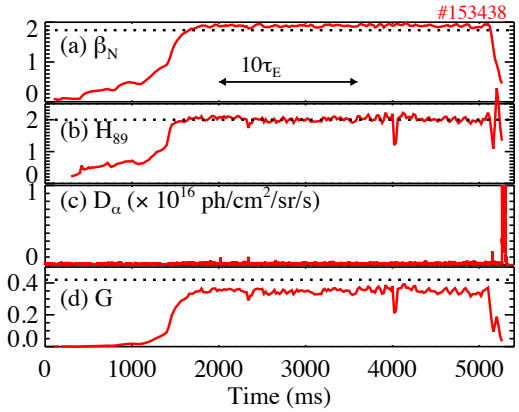

Figure 1.

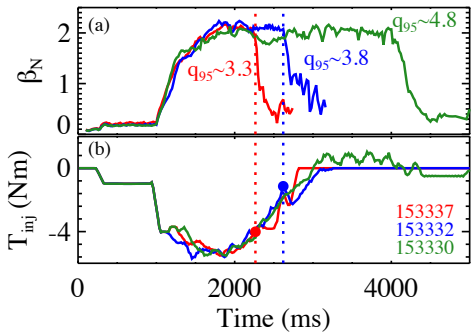

Figure 2.

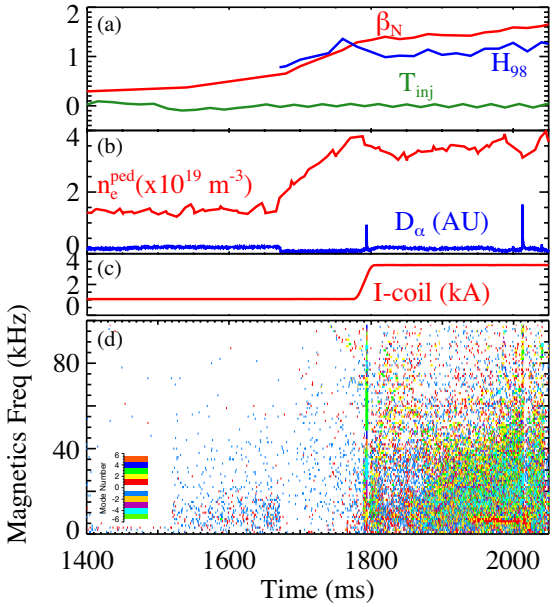

Figure 3.

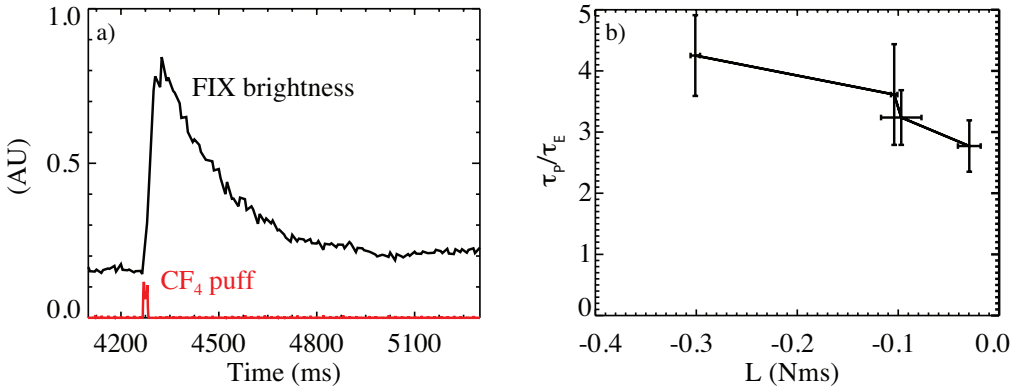

Figure 4.

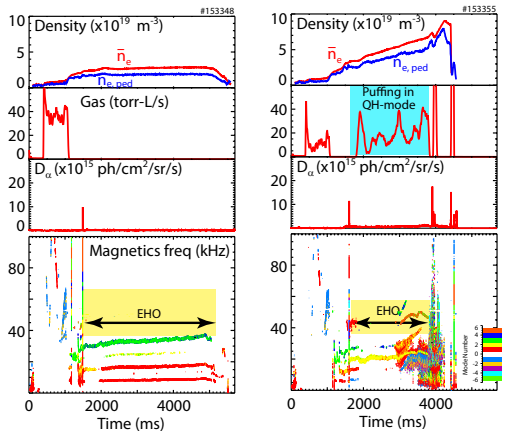

Figure 5.

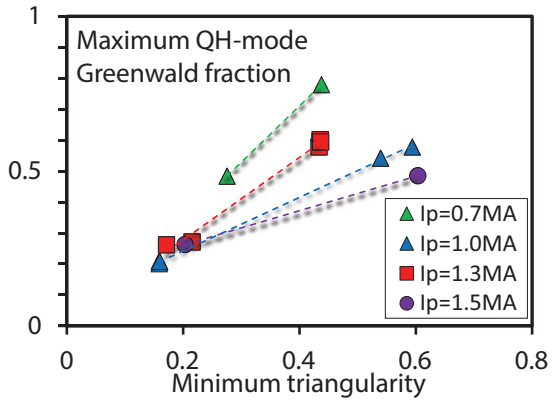

Figure 6.

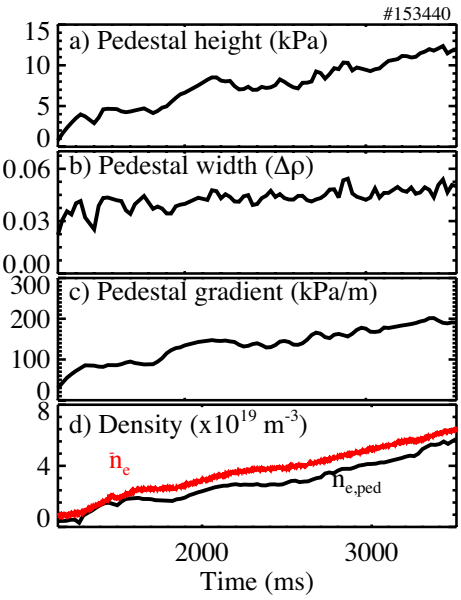
#153440
a) Pedestal height (kPa)
15
10
5
0
b) Pedestal width (Δρ)
0.06
0.03
0.00
c) Pedestal gradient (kPa/m)
300
200
100
0
d) Density (x10^19 m^-3)
8
4
0
n̄e
ne,ped
2000
3000
Time (ms)

Figure 7.

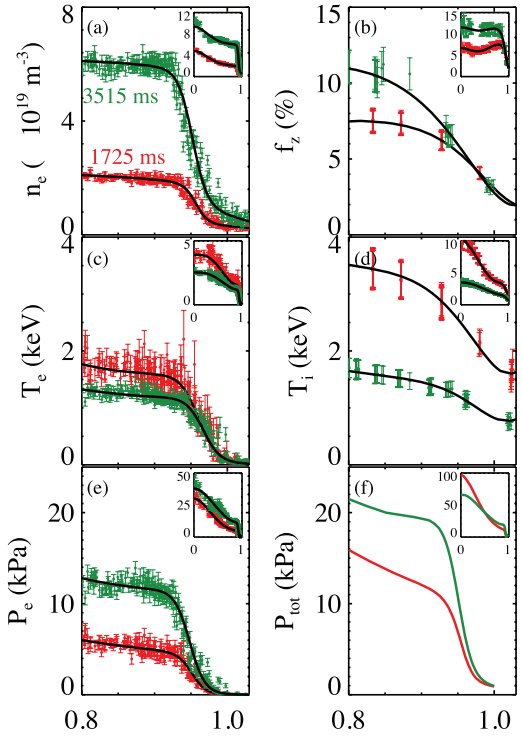
(a)
(b)
(c)
(d)
(e)
(f)
3515 ms
1725 ms
n_e (10^{19} m^{-3})
f_z (%)
T_e (keV)
T_i (keV)
P_e (kPa)
P_{tot} (kPa)
0.8
1.0

Figure 8.

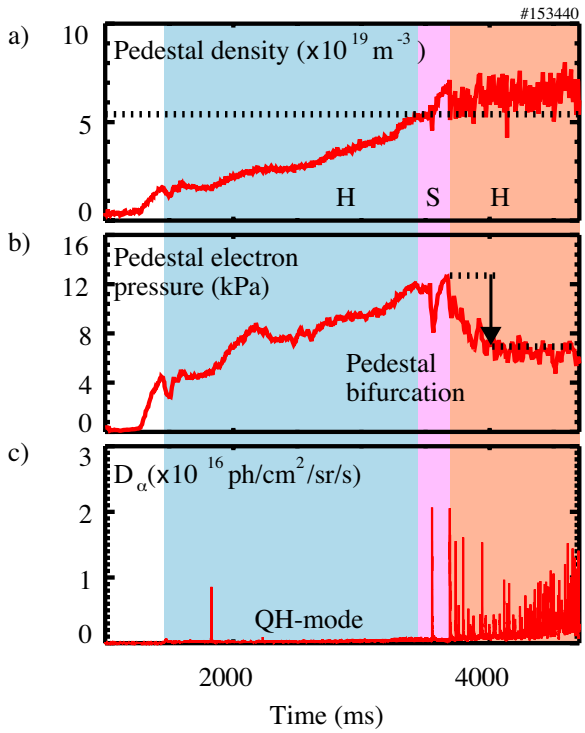
#153440
a)
Pedestal density (x10 19 m -3)
10
5
0
H
S
H
b)
Pedestal electron pressure (kPa)
16
12
8
4
0
Pedestal bifurcation
c)
D α (x10 16 ph/cm 2 /sr/s)
3
2
1
0
QH-mode
2000
4000
Time (ms)

Figure 9.

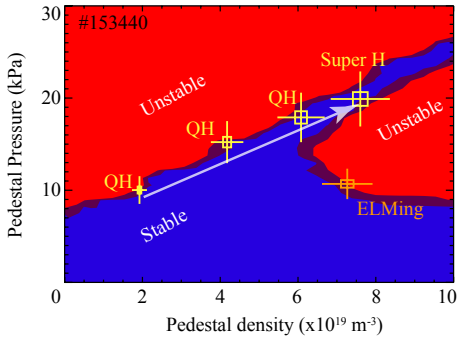
#153440
Super H
Unstable
QH
QH
Unstable
QH
ELMing
Stable
Pedestal Pressure (kPa)
Pedestal density (x10^19 m^-3)
0
2
4
6
8
10
10
20
30

Figure 10.

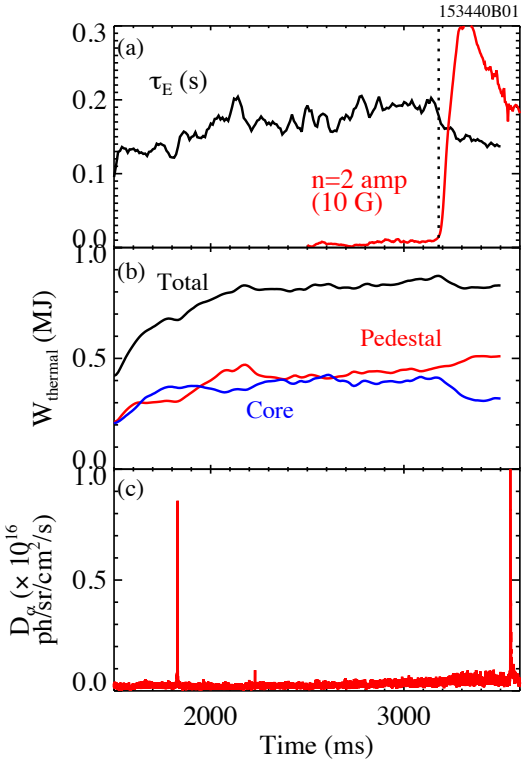
153440B01
(a)
τ_E (s)
n=2 amp
(10 G)
(b)
Total
Pedestal
Core
$W_{thermal}$ (MJ)
(c)
D_α ($\times 10^{16}$ ph/sr/cm^2/s)
Time (ms)

Figure 11.

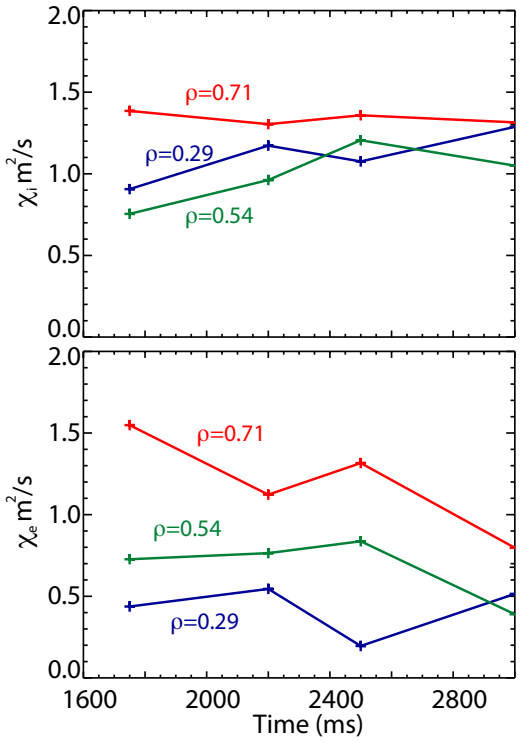
2.0
1.5
1.0
0.5
0.0
ρ=0.71
ρ=0.29
ρ=0.54
χi m2/s
2.0
1.5
1.0
0.5
0.0
ρ=0.71
ρ=0.54
ρ=0.29
χe m2/s
1600
2000
2400
2800
Time (ms)

Figure 12.

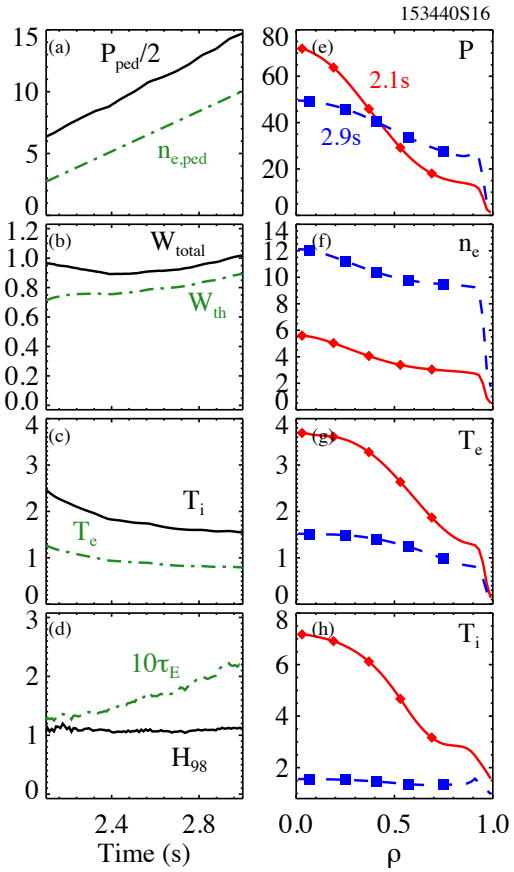
153440S16
(a)
P_ped/2
n_e,ped
(b)
W_total
W_th
(c)
T_i
T_e
(d)
10τ_E
H_98
2.4
2.8
Time (s)
(e)
P
2.1s
2.9s
(f)
n_e
(g)
T_e
(h)
T_i
0.0
0.5
1.0
ρ

Figure 13.

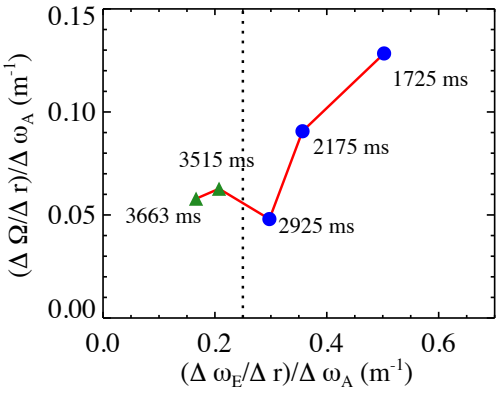

Figure 14.

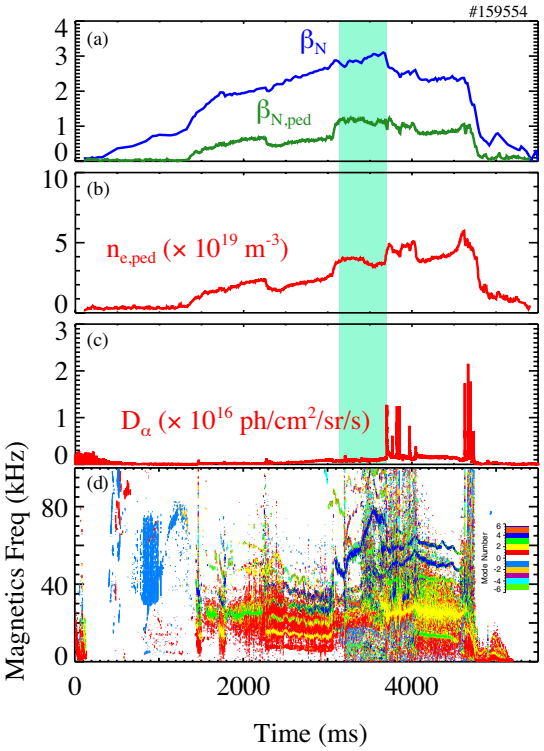

Figure 15.

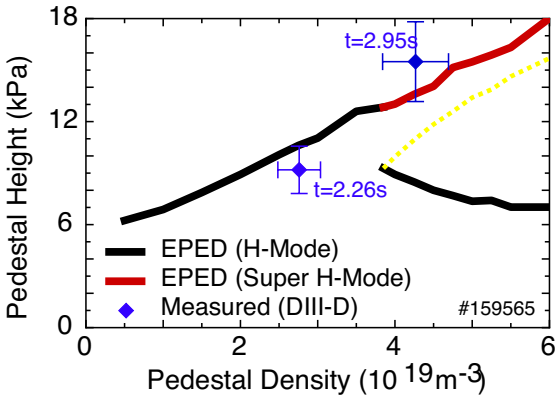
18
12
6
0
0
2
4
6
Pedestal Height (kPa)
Pedestal Density (10 19m-3)
t=2.95s
t=2.26s
EPED (H-Mode)
EPED (Super H-Mode)
Measured (DIII-D)
#159565

Figure 16.